



Ultrafast synthesis of amorphous molybdenum sulfide by magnetic induction heating for hydrogen evolution reaction

Qiming Liu^a, Forrest Nichols^a, Amrinder Bhuller^a, Kevin Singewald^a, Han-Lin Kuo^b, Jennifer Q. Lu^b, Glenn L. Millhauser^a, Frank Bridges^c, Qingfeng Ge^{d,*}, Shaowei Chen^{a,*}

^a Department of Chemistry and Biochemistry, University of California, 1156 High Street, Santa Cruz, CA 95064, United States

^b School of Engineering, University of California, 5200 North Lake Road, Merced, CA 95343, United States

^c Department of Physics, University of California, 1156 High Street, Santa Cruz, CA 95064, United States

^d School of Chemical and Biomolecular Sciences, Southern Illinois University, Carbondale, IL 62901, United States

ARTICLE INFO

Keywords:

Magnetic induction heating
Molybdenum sulfide
Amorphous
Hydrogen evolution reaction
Density functional theory

ABSTRACT

Molybdenum sulfides have emerged as viable alternatives to noble-metal catalysts for green hydrogen production via the hydrogen evolution reaction (HER). Herein, magnetic induction heating (MIH) is exploited for the rapid preparation of carbon-supported MoS_x nanocomposites. The sample prepared at 200 A for 10 s shows an amorphous Mo₃S₇Cl_y-like structure and a low overpotential (η_{10}) of −184 mV at 10 mA cm^{−2} in acidic media, whereas samples prepared at higher induction currents display a largely crystalline MoS₂ structure and drastically lower HER performance. This is due to the formation of dimeric Mo₆S₁₄ moieties in amorphous MoS_x that is facilitated by the loss of Cl residues during electrochemical reaction and enhanced H adsorption at both the S and Mo sites, in comparison to crystalline MoS₂, as shown in First-principles calculations. These results show that MIH may be used as a powerful tool in the preparation of nonequilibrium structures as high-performance electrocatalysts.

1. Introduction

Due to the ever-growing demand for energy and the rapid depletion of conventional fossil fuels, hydrogen has been hailed as one of the leading alternative energy resources for versatile applications. Nevertheless, currently hydrogen production depends mostly on the ungreen steam-methane reforming process, which is inefficient for the transition to a low-carbon economy [1]. Water electrolysis has been attracting extensive attention as a green energy technology, where hydrogen gas can be generated at the cathode by using sustainable electricity from wind, hydraulics, and solar power [2]. Yet, in electrochemical water splitting, appropriate catalysts are required to reduce the overpotential so that a sufficiently high current density can be produced for practical applications. At present, noble metal nanoparticles, such as Pt, Rh, and Ir, have been the leading catalysts for the hydrogen evolution reaction (HER), but their high costs and low natural abundances significantly hinder the wide-spread application of the technology. It is therefore of both fundamental and technological significance to develop high-performance, low-cost alternatives [3,4].

For decades, MoS₂ has been used extensively in the hydro-desulfurization (HDS) reaction, which shares a similar H* intermediate to HER [5], and the edge sites of MoS₂ are argued to exhibit a near zero Gibbs free energy (ΔG_{H^*}) of hydrogen adsorption, a condition ideal for a maximal HER activity [1,6,7]. However, experimentally, MoS₂ exhibits only a mediocre exchange current density and sluggish kinetics [1,5]. This is mainly because that, as a two-dimensional transition metal dichalcogenide, MoS₂ possesses only a minute amount of edge sites, and the dominant basal plane is inert for H adsorption. In addition, the common 2H phase of MoS₂ is semiconductive in nature, where the limited charge transport ability leads to a poor intrinsic activity. Therefore, a number of experimental strategies have been proposed to engineer the MoS₂ structure and thus to increase its HER activity. For instance, phase engineering has been employed to convert semiconductive 2H MoS₂ into metallic 1T MoS₂, resulting in enhanced current densities and reaction kinetics, with the overpotential (η_{10}) diminished to under ca. −200 mV to deliver the current density of 10 mA cm^{−2} [8]. Furthermore, defect engineering has been carried out to manipulate the material morphologies exposing specific crystal planes

* Corresponding authors.

E-mail addresses: qge@chem.siu.edu (Q. Ge), shaowei@ucsc.edu (S. Chen).

<https://doi.org/10.1016/j.apcatb.2023.123399>

Received 31 July 2023; Received in revised form 3 October 2023; Accepted 15 October 2023

Available online 17 October 2023

0926-3373/© 2023 Elsevier B.V. All rights reserved.

with edge sites by introducing vacancies, cracks, and holes on the inert basal planes [9,10]. Other strategies, such as heteroatom doping, formation of heterojunctions, and metal-support interaction on MoS₂, have also been demonstrated to be effective in increasing the HER activity [11–14].

Notably, to increase the number of active sites and hence the intrinsic activity, amorphization is a unique, efficient method [15]. For example, He et al. amorphized 2D crystalline PtSe₂ by plasma etching into disordered and metal-like PtSe_x, which exhibited a high atom-utilization efficiency of 26 wt% and a low η_{10} of −20 mV in acid [16]. In fact, various forms of amorphous MoS_x, such as MoS₄^{2−}, [Mo₂S₁₂]^{2−}, [Mo₃S₁₃]^{2−}, [Mo₃S₄]⁴⁺, and monomeric MoS₃, have been uncovered to show a high surface area and a large density of active sites [17–20]. For example, Benck et al. [21] utilized wet-chemistry synthesis to prepare amorphous MoS_x ($x = 2$ –3) nanoparticles which featured an η_{10} of ca. −200 mV and excellent stability. Seo et al. [17] synthesized polymeric chains of MoS₄^{2−} under a mild condition of wet chemistry, and observed an η_{10} of only −167 mV in acid. Wu et al. [22] showed that amorphous MoS₂ ($\eta_{10} = -210$ mV), prepared by plasma-enhanced atomic layer deposition, clearly outperformed 1T MoS₂ ($\eta_{10} = -250$ mV) and 2H MoS₂ ($\eta_{10} = -350$ mV) in acidic media, owing to the metallic conductivity with the Mo 3d orbitals crossing the Fermi level. Despite much progress, it should be noted that synthesis of amorphous MoS_x mostly requires either unconventional plasma etching or long-term wet chemistry, which is non-sustainable and time-consuming. This is partly due to the meta-stable nature of amorphous MoS_x, which is difficult to attain under conventional treatment.

Recently, magnetic induction heating (MIH) has been used to prepare materials of meta-stable/nonequilibrium structures within seconds, e.g., FeNi spinels with a good mixing of the Fe and Ni phases [23], Ru nanoparticles with metal-Cl residues [24], and defective Co-N carbon nanocomposites [25], which are impossible to achieve with conventional synthetic methods [26,27]. This is because MIH can heat up samples at an ultrafast rate up to 200 K s^{−1}, due to the Joule heating of Eddy current from high-frequency electromagnetic fields. Herein, a series of carbon-supported MoS_x nanocomposites were prepared by MIH treatment of MoCl₅ and thiourea at controlled currents for 10 s. Among the series, the sample prepared at a relatively low induction current of 200 A showed an amorphous structure and the best HER performance in acidic media, with a low η_{10} of only −184 mV and fast electron-transfer kinetics with a low Tafel slope of 50 mV dec^{−1}, whereas samples prepared at higher induction currents display mostly a crystalline MoS₂ structure and a much lower performance ($\eta_{10} = -340$ mV). Computational studies based on density functional theory (DFT) calculations confirm the metallic nature of the amorphous MoS_x, and both the Mo and S sites of the Mo₃-based sulfide clusters may serve as the active sites. In particular, Mo₆S₁₄ clusters were likely the dominant species responsible for the HER activity, with the formation facilitated by the loss of Cl residues during electrochemical reactions. Analysis of the projected density of states (PDOS) shows that H adsorption on these MoS_x affects the stability of the system by altering the antibonding states of S-H and Mo-S, and hence impacting the adsorption energetics. Overall, results from this study show that MIH can be used as a powerful tool to prepare meta-stable materials as high-performance electrocatalysts.

2. Experimental section

2.1. Chemicals

Molybdenum(V) chloride (MoCl₅, 95%, ACROS Organics), thiourea (CH₄N₂S, 99.0%, Sigma-Aldrich), carbon black (Vulcan XC72), ethanol (Fisher Chemicals), and Pt/C (20 wt%, Alfa Aesar) were used as received without further purification. Water was purified with a Barnstead Nanopure Water System (18.2 MΩ cm).

2.2. MIH synthesis

25 mg of MoCl₅ and 25 mg of thiourea were dissolved in 5 mL of ethanol under sonication to produce a transparent solution, into which was then added 50 mg of carbon black. The mixture was dried by rotary evaporation and further desiccated in a vacuum oven at 60 °C for 8 h, before being loaded onto an iron sheet (2.5 cm × 2.5 cm × 0.2 mm) covered with a piece of graphite paper (0.01 mm thick) to prevent contamination from iron. The assembly was then placed onto the center of a firebrick inside a quartz tube and purged with high-purity Ar gas for 10 min. The quartz tube was placed in a four-turn induction coil with a diameter of 5 cm, and MIH was carried out at a controlled current ($X = 100, 200, 300, 400$, and 600 A) for a heating time of 10 s before the sample was naturally cooled down to room temperature. The resulting samples were denoted as MS-X.

2.3. Characterizations

Transmission electron microscopy (TEM) images were acquired with a Tecnai G2 operated at 200 kV. X-ray photoelectron spectroscopy (XPS) measurements were carried out with a Thermo Fisher K-alpha system, where the binding energy was calibrated against the C 1s binding energy. Raman measurements were conducted using a Horiba Jobin Yvon LabRAM ARAMIS automated scanning confocal Raman microscope under 532 nm excitation. Continuous wave-electron paramagnetic resonance (CW-EPR) measurements were carried out with a Bruker EleXsys E580 EPR spectrometer at the X-band frequency (~9.857 GHz) using an ER 4122SHQE resonator. All CW-EPR spectra were recorded using a power of 2 mW, a modulation amplitude of 4 G, a modulation frequency of 100 KHz, a conversion time of 20.48 ms, and the number of scans of 10. Ex situ X-ray absorption spectroscopy (XAS) measurements were carried out at 10 K at beamline 4-1 of the Stanford Synchrotron Radiation Lightsources using an Oxford liquid helium cryostat. The fitting of XAS data was done by using Real-Space X-ray Absorption Package (RSXAP) [28].

2.4. Electrochemistry

Electrochemical measurements were carried out with a CHI 700E electrochemical workstation in a three-electrode configuration. A glassy carbon electrode (3 mm in diameter) was used as the working electrode. A graphite rod was used as the counter electrode and an Ag/AgCl (in 3 M KCl) as the reference electrode. The reference electrode was calibrated against a reversible hydrogen electrode (RHE) and all potentials in the present study were referenced to this RHE. Commercial Pt/C was dropcast onto the glassy carbon electrode at a loading of 40 μg cm^{−2} for benchmarking.

2.5. Computational study

First-principles computations were performed using Quantum ESPRESSO, an open-source plane-wave code [29]. A super cell with the unit size of 15 × 15 × 15 Å³ was used for Mo₃S₇Cl_y ($y = 0, 2, 4, 6$) clusters and 20 × 15 × 15 Å³ for Mo₆S₁₄. The shortest distance between the atoms in the neighboring periodic images was at least 9 Å. MoS₂ basal plane was built on 2H-MoS₂ (001) facets with two layers and 54 atoms in total. The bottom layer was fixed during the geometry relaxation. The MoS₂ edge was built on the 2H-MoS₂ (100) facets with four layers and 72 atoms in total. The bottom two layers were fixed during the geometry optimization. At least 10 Å vacuum was inserted between the periodic images to minimize the spurious interactions between the images. The GBRV ultrasoft pseudopotentials with a cutoff energy of 50 and 500 Ry for kinetic energy and charge density, respectively, were chosen [30]. Grimme's D3 dispersion corrections were used in the calculation of MoS₂ basal planes and edges [31]. Fermi-level smearing with a Gaussian width of 1 × 10^{−4} eV was used to accelerate the

self-consistent total-energy iterations. Monkhorst-Pack K-point grids of $3 \times 2 \times 1$ for the edge of MoS_2 and $2 \times 2 \times 1$ for the basal plane of MoS_2 were selected and scf cycles were converged at 1 meV per atom. For geometry optimizations, the convergence was 10^{-8} Ry of the electronic energy and 10^{-4} au for the total force. Density functional perturbation theory was employed to calculate the frequencies. Entropy and zero-point energy were determined based those frequencies [32]. Raman spectra were calculated using Gaussian 16 with the PBE functional on the relaxed cluster structures without further optimization [33]. The effective core potential and basis set, ECP28MDF_AVTZ [34], was adopted for Mo and the aug-cc-pvtz basis sets were used for all other elements.

3. Results and discussion

3.1. Sample preparation

The preparation process of MoS_x is schematically illustrated in Fig. 1, which consists of two major steps. First, MoCl_5 and thiourea (Fig. 1b) were co-dissolved in ethanol to form a clear solution, and the solution was mixed with carbon black, which was then placed onto a boat-like iron sheet and positioned inside a quartz tube purged with Ar gas (Fig. 1a). Finally, the entire assembly was placed in the center of an induction coil and thermally treated at a controlled AC current. The temperature of the iron sheet was recorded using an infrared thermometer as a function of induction current and heating time, as depicted in Fig. 1c. The heating rate was estimated to be ca. 200°C s^{-1} at 600 A and ca. 40°C s^{-1} at 100 A, significantly higher than that with a conventional tube furnace or by hydrothermal methods [25]. During the MIH treatment, the instantly generated Eddy current quickly heats up the surface of the iron sheet to the desired temperature within seconds due to the Joule's heating effect, where the precursors underwent rapid decomposition into different forms of MoS_x as a function of the induction currents. Five samples were prepared at an MIH current (X) up to 600 A for 10 s and denoted as MS-X (X = 100, 200, 300, 400, and 600).

3.2. Structural characterization

The morphologies of the samples were first characterized by TEM measurements. One can see from Fig. S1 that MS-100 displayed a sheet-like structure, which spanned hundreds of nanometers, and no well-defined lattice fringes at high resolutions, implying that MS-100 was mostly amorphous in nature, possibly due to the relatively low heating current (100 A)/low temperature and hence limited decomposition of the precursors. At a higher heating current of 200 A, MS-200 manifests an irregular morphology, consisting of stacks of nanosheets with widths of ca. 60 nm (Fig. S2), and also exhibits no well-resolved lattice fringes (Fig. 2a-b). In fact, no clear patterns can be found in the corresponding Fast Fourier Transform (FFT) image (Fig. S3), further confirming its amorphous nature. By contrast, MS-300 can be found to consist of an agglomerate of both amorphous and crystalline nanoparticles (Fig. S4a), and the latter exhibited clearly-defined lattice fringes (Fig. S4b-d), with two interplanar distances of 0.26 and 1.04 nm due to the (100) and expanded (002) facets of 2H MoS_2 , respectively [35,36]. As for MS-400, MoS_2 nanosheets can be clearly observed (Fig. 2c and S5), as the interlayer spacings of 0.68 nm is consistent with the (002) facets of 2H MoS_2 [37]. When the MIH current was increased further to 600 A, the sheet structure became even better defined (Fig. 2d and S6), where the d spacings of 0.24 and 0.27 nm can be ascribed to the (104) and (100) facets of 2H MoS_2 , respectively [38,39]. These results suggest that the sample morphologies can be readily regulated by the magnetic induction currents. At low currents (under 200 A), the relatively low heating temperatures produced a mostly amorphous structure; and at 300 A, crystalline MoS_2 started to appear, which became the dominant species at higher induction currents (i.e., 400 and 600 A).

Notably, elemental mapping analysis based on energy-dispersive X-ray spectroscopy (EDS) showed that for MS-200, the elements of Mo, S, and Cl were evenly distributed across the amorphous sheet (Fig. 2e), suggesting residual Cl in the sample likely in the form of MoS_xCl_y , a marked deviation from the crystalline MoS_2 produced at higher currents/temperatures. In fact, from the EDS analysis (Fig. S7), the Mo:S:Cl ratio was estimated to be ca. 1:1.9:1, implying that MS-200 was most

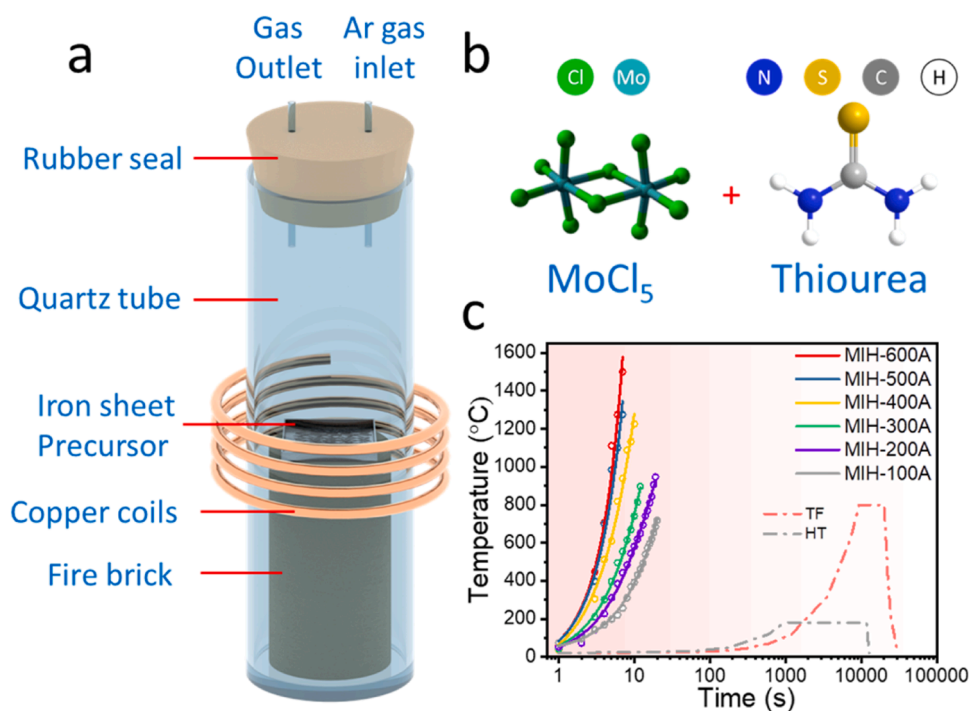


Fig. 1. (a) Scheme of MIH setup. (b) Precursors of MoCl_5 and thiourea for the synthesis of the MoS_x samples. (c) Heating temperature as a function of time at different induction currents, as determined with an infrared thermometer [25]. TF and HT denote conventional tube furnaces and hydrothermal methods, respectively.

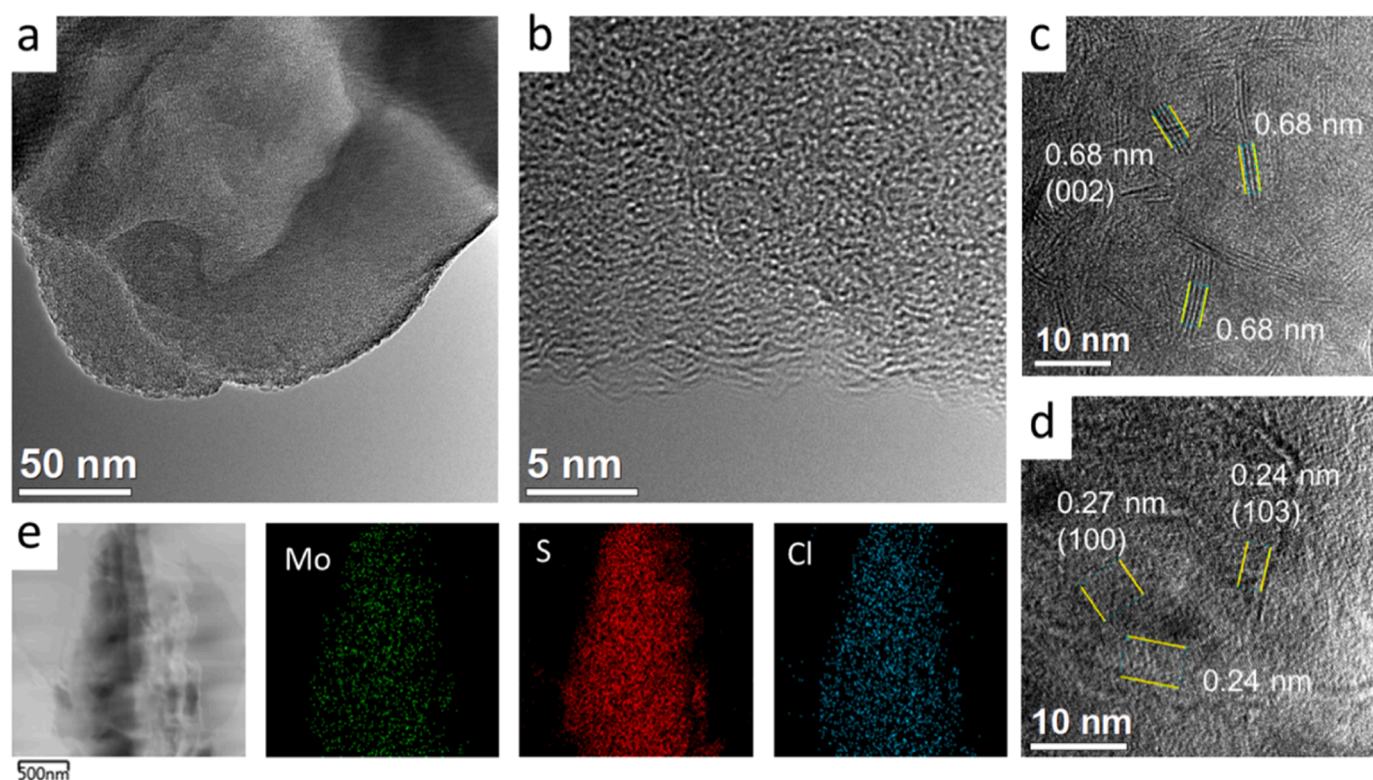


Fig. 2. (a, b) Representative TEM images of MS-200, (c) MS-400, and (d) MS-600. (e) EDS-based Elemental mapping analysis of Mo, S, and Cl in MS-200.

likely a meta-stable intermediate during the decomposition of the precursors, owing to the moderate heating temperature [40].

XPS measurements were then performed to examine the chemical compositions and valence states of the samples. From the survey spectra in Fig. S8, one can see that the C 1s, N 1s, O 1s, S 2p, Cl 2p, and Mo 3d electrons can be readily identified at 284, 400, 532, 164, 198, and 231 eV, respectively, in all samples. Fig. 3a shows the high-resolution scans of the Mo 3d electrons. In comparison to the MoCl_5 precursor that featured a $3d_{5/2}/3d_{3/2}$ doublet at 230.78/233.96 eV (the single peak at 227.10 eV is due to the S 2s electrons of thiourea) [41,42], all MIH-treated samples exhibited a marked red-shift. Specifically, for MS-300, MS-400 and MS-600, the binding energies of the Mo $3d_{5/2}/3d_{3/2}$ doublet red-shifted by over 1.5 eV to 229.21/232.37, 229.14/232.32, and 229.10/232.25 eV, respectively, which are consistent with those for Mo^{4+} [43,44]; whereas for MS-200 and MS-100, the red-shift diminished somewhat to ca. 1.0 eV, 229.74/232.91 eV for MS-100, and 229.67/232.82 eV for MS-200, suggesting partial decomposition (reduction) of Mo^{5+} to a meta-stable structure with a valence state close to 4+ [17]. These binding energies are all listed in Table S1.

Consistent results were obtained from the high-resolution scans of the S 2p electrons, which further confirmed the formation of MoS_x in the samples. One can see from Fig. 3b that the MoCl_5 + thiourea precursors possessed two doublets at 162.07/163.14 and 163.82/164.99 eV (Table S1), which can be assigned to the S $2p_{3/2}/2p_{1/2}$ electrons of Mo-S and thiourea, respectively, suggesting the formation of Mo-Cl/thiourea complexes in the precursor solution [45]. These two doublets remained rather visible for MS-100 (162.32/163.58 and 163.48/164.70 eV) and MS-200 (162.28/163.54 eV and 163.56/164.79 eV), in good accord with the incomplete decomposition of the precursors into MoS_x . Note that these two doublets are rather consistent with the terminal S_2^{2-} (blue-shaded peaks) and bridging/apical S_2^{2-} (yellow-shaded peaks) of $[\text{Mo}_3\text{S}_{13}]^{2-}$ clusters (Fig. S9) and amorphous MoS_3 , but deviate markedly from those of crystalline MoS_2 [17, 20,46,47]. For samples prepared at higher heating currents, they all manifested only one doublet at somewhat lower binding energies,

162.01/163.25 eV for MS-300, 161.98/163.21 eV for MS-400, and 161.97/163.20 eV for MS-600. The fact that the higher-energy doublet vanished suggests (a) complete thermal decomposition of the thiourea precursor at high temperatures, (b) diminishing bridging S dimers, and (c) formation of crystalline MoS_2 , in agreement with the above TEM results [22]. In fact, in comparison to the S:Mo feed ratio of 3.55 in the precursors, the atomic ratio of S to Mo (Table S2) can be found to decrease to 3.38 for MS-100, 2.95 for MS-200, 2.10 for MS-300, 2.36 for MS-400, and 2.04 for MS-600. Again, this is in agreement with only incomplete decomposition of precursors in MS-100 and MS-200, whereas the MS-300, MS-400 and MS-600 mostly entailed the stoichiometric formation of MoS_2 in the samples.

A similar diminishing trend can be found in the Cl 2p spectra. From Fig. 3c, one can clearly see all samples (except for MS-600) displayed a doublet around 198/199 eV, which can be ascribed to Mo-Cl [24,40]. In fact, one can see that the precursors, MS-100, and MS-200 all showed a doublet at 197.70/199.30 eV, while for MS-300 and MS-400, the binding energies of the doublet blue-shifted to 198.13/199.70 eV and 198.66/200.36 eV (Table S1), possibly due to the reduced interaction between the Cl and Mo species [24], and for MS-600, the Cl completely vanished, suggestive of thermal instability of the Mo-Cl species at high heating temperatures. Similar to the S content, the atomic ratio of Cl to Mo (Table S2) decreased from 2.02 for the precursors to 1.32 for MS-100, 1.29 for MS-200, and then drastically to only 0.21 for MS-300 and 0.15 for MS-400, and finally to virtually zero for MS-600. These results further confirmed that MS-100 and MS-200 consisted mostly of the meta-stable MoS_xCl_y during the decomposition of the precursors, whereas crystalline MoS_2 was produced in MS-300, MS-400 and MS-600.

The high-resolution scans of C 1s, O 1s, and N 1s also provide important structural information during the ultrafast synthesis of MoS_x . One can see from Fig. S10 that all samples consisted of three major peaks at ca. 284.15, 285.40, and over 288 eV, which can be assigned to C=C, C-C, and oxidized C of the carbon black supporting substrates [25,48]. As for O 1s in Fig. S11, all samples exhibited two major peaks at ca. 531

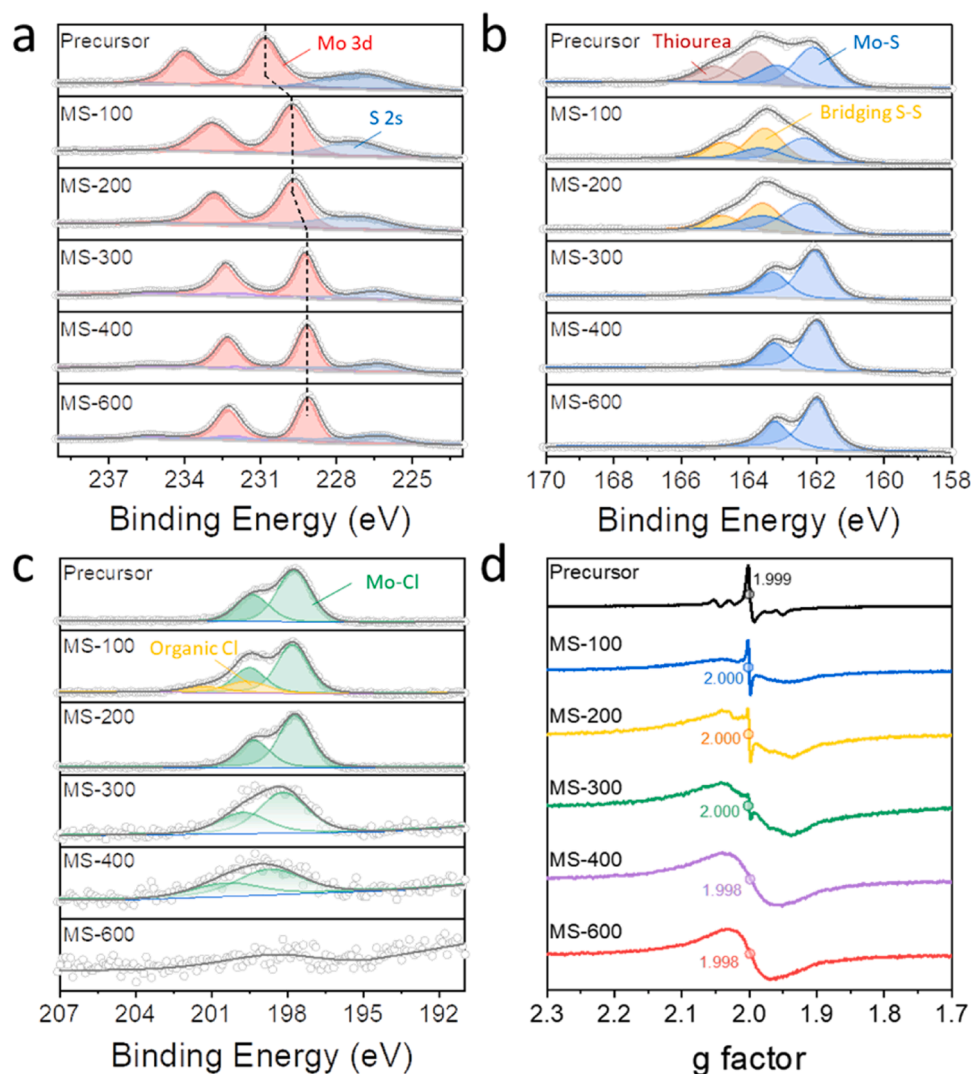


Fig. 3. High-resolution XPS scans of the (a) Mo 3d, (b) S 2p, and (c) Cl 2p electrons of MS-100, MS-200, MS-300, MS-400, MS-600, and the precursors of MoCl_5 + thiourea. (d) CW-EPR spectra and g factors of the sample series.

and 532 eV, which originated from the C=O and C-O on the carbon matrix, respectively [25,48,49]. It should be noted that no peaks under 530 eV can be discerned in the spectra, indicating the absence of metal oxides in the samples likely due to the good protection of the Ar atmosphere during sample preparation [50]. As for the N 1s spectra in Fig. S12, one can find that the N peak (the adjacent peak at a lower binding energy is due to Mo $2p_{3/2}$) shifted from 399.74 eV for the precursor to 399.21 and 399.30 eV for MS-100 and MS-200, and further to 398.67, 397.98, 398.13 eV for MS-300, MS-400, and MS-600, respectively, suggesting that the amino groups ($-\text{NH}_2$) of thiourea were thermally converted into pyridinic N embedded within the carbon matrix [48]. Mo $2p_{3/2}$ also consistently follows the diminishing trend of the Mo 3d spectra. Meanwhile, it should be noted that no nitride peaks can be deconvoluted in N 1s spectra, ruling out the formation of MoN_x species [51]. These data are listed in Table S1-S2.

Further structural insights were obtained from CW-EPR measurements. One can see from Fig. 3d that the precursor displayed a series of sharp signals that are consistent with penta-coordinated Mo^{5+} , with a g factor of 1.999 [52]. As for MS-100 and MS-200, the sharp peaks all became attenuated and broadened, with the g factors changed slightly to 2.000, implying a coordination structure similar to that of MoS_3 [53,54]. The sharp signals became further attenuated for MS-300 and completely disappeared for MS-400 and MS-600, with only a broad linewidth and a

g factor of 1.998, suggesting that Mo^{5+} was fully reduced to Mo^{4+} in crystalline but defective MoS_2 , which are consistent with the above XPS and TEM results. It should also be noted that the signal intensity gradually decreased for the samples prepared at higher induction currents (Fig. S13), signifying a decreasing density of defects with increasing MIH temperature [10].

Consistent results were obtained in Raman spectroscopies measurements which showed the gradual evolution of the Mo-S vibrations among the samples. As depicted in Fig. 4a, the precursor showed three peaks at 284, 337, and 377 cm^{-1} , which can be ascribed to the E_{1g} , A_1 , and E_{2g}^1 vibrations of the Mo-S/Cl bonds in the Mo-thiourea complex, respectively [47,55]. As for MS-100 and MS-200, in addition to the 291 and 341 cm^{-1} vibrations, two new peaks appeared at 363 and 393 cm^{-1} (gray-shaded area, Fig. 4a), which blue-shifted gradually to higher frequencies with increasing MIH currents, at 378 and 401 cm^{-1} for MS-300, 381 and 404 cm^{-1} for MS-400, and 382 and 406 cm^{-1} for MS-600, and became increasingly consistent with those of crystalline MoS_2 [8,56]. This suggests that (a) the bond length of Mo-S is somewhat longer for samples prepared at a lower heating temperature; and (b) MS-300 likely consisted of a mix of amorphous and crystalline MoS_x , while at 400 and 600 A, crystalline MoS_2 is the dominant product [57].

To further understand these vibrational properties, the vibrational spectra of $\text{Mo}_3\text{S}_7\text{Cl}_4$, Mo_3S_6 , and $\text{Mo}_3\text{S}_{12}\text{H}_6$ were calculated by using the

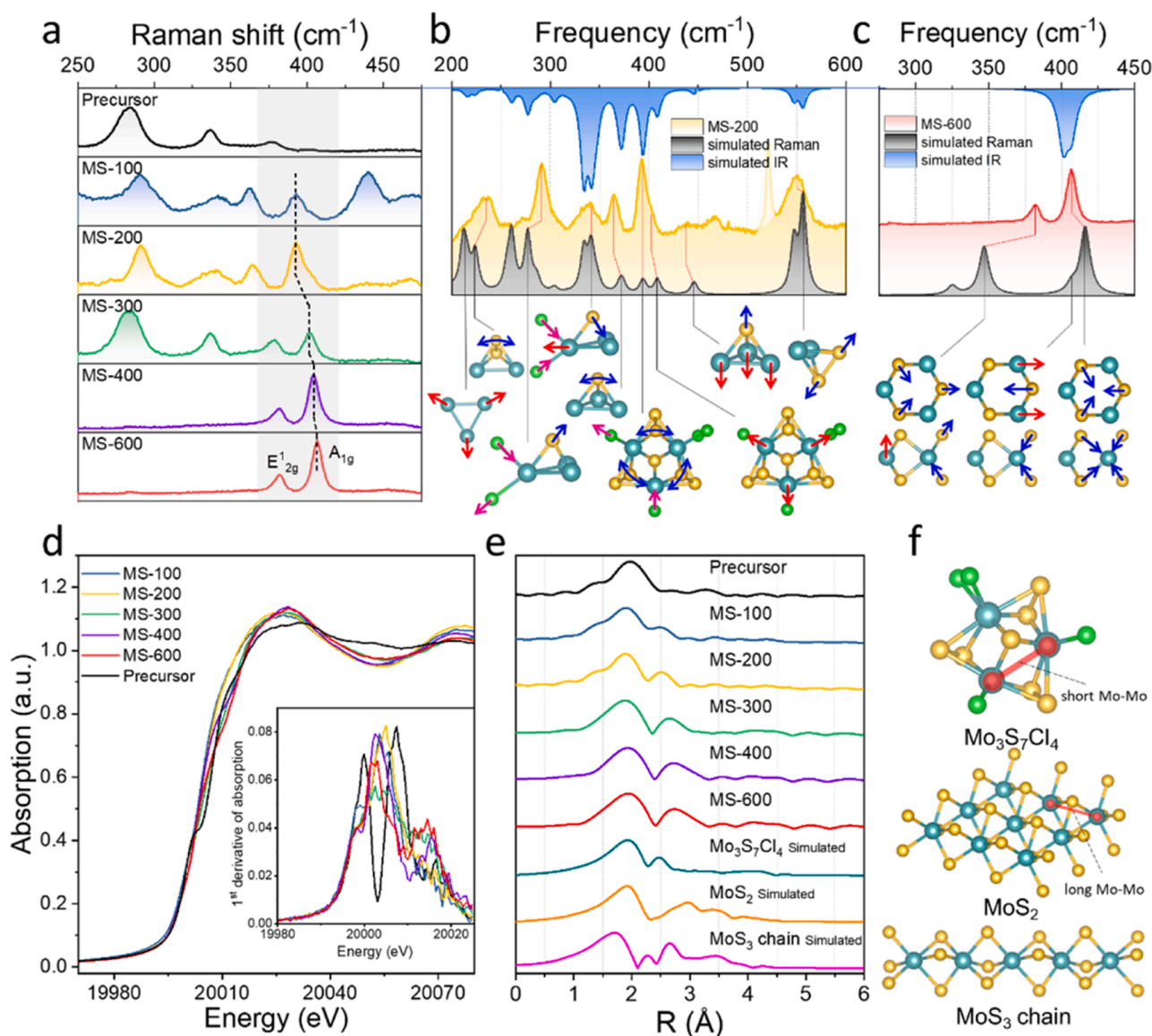


Fig. 4. (a) Raman Spectra of precursors, MS-100, MS-200, MS-400, and MS-600. Simulated Raman and IR spectra of (b) Mo₃S₇Cl₄ and (c) Mo₃S₆ clusters, in comparison to the experimental data of MS-200 and MS-600. (d) Mo K-edge X-ray absorption near-edge spectra (XANES) of precursor, MS-100, MS-200, MS-400, MS-600, the inset is the 1st derivative of the curves. (e) Mo K edge Fourier-transformed extended X-ray absorption fine structure spectra (FT-EXAFS). Note that panel (e) includes simulated EXAFS for (f) Mo₃S₇Cl₄, 2H-MoS₂, and monomeric MoS₃ chain. The colors of elements are cyan for Mo, yellow for S, and green for Cl.

Gaussian program (Fig. 4b-c and S14-S17, and Video S1-S3). Fig. 4b depicts the theoretical vibration spectra (blue and grey curves) and vibrational modes (Video S1) of Mo₃S₇Cl₄, in comparison to the experimental Raman spectrum of MS-200 (orange curve). The peak observed experimentally at 234 cm⁻¹ for MS-200 is likely due to the vibrations of the Mo trimer and bridging S₂ of Mo₃S₇Cl₄ which are predicted to be at 212 and 224 cm⁻¹, whereas the peak at 291 cm⁻¹ is rather close to the Mo-Cl and apical S vibrations (predicted at 277 cm⁻¹). Additional peaks can be found at 341, 373, 394, 409, and 438 cm⁻¹ in the simulated spectra and that of MS-200, due to the hybrid vibrations of Mo-Cl, apical S, bridging S₂, and Mo trimer. Furthermore, one can see that MS-200 exhibited a clearly defined peak at 552 cm⁻¹, almost identical to the calculated one (556 cm⁻¹) for S-S bonds in bridging S₂. Notably, the vibrational peaks of bridging S₂ can only be observed with MS-100 and MS-200 (Fig. S18), which is consistent with results from the above XPS measurements, as they are associated with amorphous MoS₃ rather than crystalline (2H) MoS₂ [58,59]. Interestingly, the calculated spectrum of the Cl-free Mo₃S₁₂H₆ (Fig. S16-S17 and Video S2) deviates apparently

from that of MS-100 or MS-200, displaying no vibrations from apical S or bridging S₂. In fact, the experimental Raman patterns of MS-100 and MS-200 are similar to those of coordination polymers consisting of discrete [Mo₃S₁₃]²⁻ building blocks reported previously [20,53]. For comparison, MS-600 displays only two major peaks at 346 and 416 cm⁻¹, due to Mo-S vibrations, and no additional vibrations from bridging S₂ or Mo trimer vibrations, in agreement with the simulated results of Mo₃S₆ which consists of blocks of crystalline MoS₂ (Fig. 4c and S15, Video S3). Taken together, these results suggest that the atomic structure of MS-100 and MS-200 resembled that of the Mo₃S₇Cl₄ cluster, due to only partial decomposition of the precursors, whereas for samples prepared at higher induction currents, the structure became increasingly close to that of Mo₃S₆. This is consistent with the amorphous to crystalline structural evolution with induction current observed above in XPS, TEM, and CW-EPR measurements.

Supplementary material related to this article can be found online at [doi:10.1016/j.apcatb.2023.123399](https://doi.org/10.1016/j.apcatb.2023.123399)

XAS studies were then performed to further understand the valence

state and atomic structure of the MoS_x samples. One can see from the Mo K-edge X-ray absorption near edge structure (XANES) spectra in Fig. 4d that the precursors displayed a pre-edge feature at ca. 20002 eV, due to the 1s-4d transition of the tetrahedral symmetry [60]. This pre-edge feature diminished after MIH treatments, implying its ready decomposition. It should be noted that MS-100 and MS-200 showed a similar absorption edge and hence a similar chemical environment, whereas MS-300, MS-400, and MS-600 constituted a separate group that exhibited also a similar edge, possibly due to the loss of Cl residuals and increasing crystallization which altered the atomic symmetry of Mo [22]. This is consistent with the above XPS results. The first derivatives of XANES are shown in the inset to Fig. 4d, which entailed a series of peaks with the energies decreasing in the order of precursor > MS-100 > MS-200 > MS-300 > MS-400 > MS-600. This suggests that the samples indeed became increasingly reduced with increasing heating currents, in line with the XPS results.

The corresponding Fourier-transform extended X-ray absorption fine structure (FT-EXAFS) spectra further confirmed the structural evolution of the samples. It can be seen from Fig. 4e that the precursors possessed only one main peak at 1.96 Å, due to the Mo-S/Cl path [22,61,62], whereas for the MIH-treated samples, in addition to the dominant peak at ca. 1.90 Å, additional peaks emerged at higher energies, due to the Mo-Mo bonds [17,22,61]. For MS-100 and MS-200, the Mo-Mo peak appeared at 2.50 Å, analogous to that of Mo₃S₇Cl₄ with a short Mo-Mo bond as simulated by FEFF7 (Fig. 4f), consistent with the Raman simulation [63]. This peak shifted to 2.65 Å for MS-300, and 2.72 Å for both MS-400 and MS-600, which was close to that of simulated 2H MoS₂ with long Mo-Mo bonds (Fig. 4f). It should be noted that no peaks can be discerned at 1.5 Å, meaning no formation of either oxides or nitrides, consistent with the above XPS results. Fitting of the FT-EXAFS spectra (Fig. S19, Table S3-S8) showed that MS-100 and MS-200 possessed a Mo-S/Cl bond length of 2.43 Å, with the corresponding coordination number (CN) of 4.0 and 4.9, in comparison to that of the precursor

(2.46 Å, CN = 2.1). The Mo-S/Cl bond length decreased to 2.39, 2.40, and 2.39 Å for MS-300, MS-400, and MS-600, respectively. In fact, the result is consistent with the blueshift of the vibrational energies (Fig. 4a). It should be noted that they all have relatively low CNs of Mo-S/Cl as compared to that of ideal MoS₂ (CN = 6), implying a high density of defects in the samples [64]. The fittings of the Mo-Mo bonds showed that the bond lengths for MS-100 and MS-200 are 2.69 and 2.73 Å, respectively, which are almost identical to the shorter Mo-Mo bonds in Mo₃S₇Cl₄ or [Mo₃S₁₃]²⁻ [17,22]. The Mo-Mo bonds further increased to 3.14 Å for MS-300, and 3.16 Å for both MS-400 and MS-600, consistent with that of crystalline MoS₂. Notably, the simulated FT-EXAFS of the monomeric MoS₃ chain (Fig. 4f) shows peaks unlike those of MS-100 or MS-200, ruling out the monomeric structure in the samples [47]. Therefore, MS-100 and MS-200 can be seen to consist of an amorphous structure similar to that of Mo₃S₇Cl₄, whereas MS-300, MS-400, and MS-600 entail mostly crystalline MoS₂, consistent with the TEM, XPS, CW-EPR, and Raman results.

3.3. Electrochemical study

The HER polarization curves of the samples were then acquired in 0.5 M H₂SO₄. One can see from Fig. 5a that MS-200 emerged to be the best catalyst among the series of samples, with the lowest η_{10} of -184 mV, as compared to -217 mV for MS-100, -232 mV for MS-300, -243 mV for MS-400, and -244 mV for MS-600. From Fig. 5b one can see that MS-200 also possessed the lowest Tafel slope of 50.0 mV dec⁻¹, and MS-100 displayed a similar one of 55.3 mV dec⁻¹; yet the slopes increased drastically to 69.9, 77.2, and 82.5 mV dec⁻¹ for MS-300, MS-400, and MS-600, respectively, suggesting increasingly sluggish electron-transfer kinetics. Such a discrepancy may be ascribed to the amorphous-crystalline structural evolution of the samples with induction current. That is, the abundant defects in MS-100 and MS-200 most likely facilitated H adsorption, such that the Heyrovsky reaction acted as

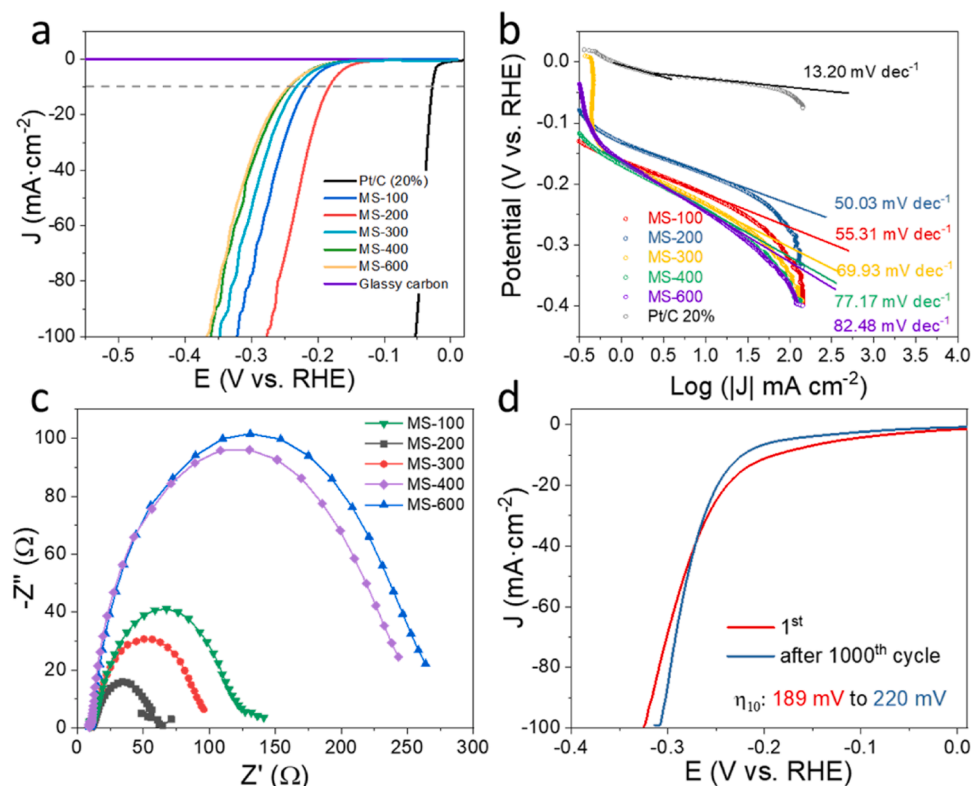


Fig. 5. (a) HER polarization curves of the samples, commercial Pt/C, and bare glassy carbon at a scan rate of 10 mV s⁻¹ in 0.5 M H₂SO₄. (b) The corresponding Tafel plots of the sample series. (c) Nyquist plots of the sample series from electrochemical impedance spectroscopy (EIS) measurements at an overpotential of -200 mV. (d) Stability tests of the best sample MS-200.

the rate-determining step (RDS) of HER [65–68], whereas for the mostly crystalline samples of MS-300, MS-400 and MS-600, the HER performance became increasingly limited by the Volmer step [67], as the dominant basal planes are mostly inactive for H adsorption [69]. Therefore, whereas the performance remains subpar as compared to that of commercial Pt/C ($\eta_{10} = -28$ mV, Tafel slope = 13.2 mV dec $^{-1}$), these results did highlight the significance of MIH in the effective preparation of defective/amorphous MoS $_x$ in reducing the HER overpotentials.

Consistently, electrochemical impedance spectroscopy (EIS) measurements (Fig. 5c) showed that MS-200 possessed the lowest charge-transfer resistance (R_{ct}) of 45.2Ω at the overpotential of -200 mV, in comparison to 109.6Ω for MS-100, 79.76Ω for MS-300, 232.9Ω for MS-400, and 254.6Ω for MS-600. The enhanced charge-transfer kinetics can be ascribed to the structural transition from the semiconductive crystalline MoS $_2$ to the metallic amorphous MoS $_x$ [22]. The electrochemical surface area (ECSA) of the samples was then assessed by measuring the double layer capacitance (C_{dl}), which remained rather close among the series (Fig. S20, Table S9), suggesting that the HER performance of the samples was primarily dictated by the intrinsic activity of the active sites, rather than the ECSA. The corresponding turnover frequency (TOF) is shown in Fig. S21, where MS-200 exhibited the highest TOF (ca. 0.55 s $^{-1}$ at -0.20 V), followed by MS-200, MS-300, MS-400 and MS-600.

The amorphous MS-200 also exhibited excellent stability towards HER. From Fig. 5d, one can see that after 1000 cycles of potential scans, the η_{10} shifted from -189 mV to -220 mV, but the current densities became even higher at higher overpotentials (at potentials over -270 mV). XPS measurements (Fig. S22a) showed two doublets at $229.74/232.79$ eV and $231.92/234.97$ eV, which can be assigned to the Mo 3d electrons of MoS $_x$ and oxidized Mo, respectively (the latter possibly due to the loss of Cl residues and the replacement by aqua/hydroxo ligands, vide infra) [46]. As for S 2p (Fig. S22b), two components can be resolved at $162.51/163.77$ eV for S in MoS $_x$ and

$168.08/192.15$ eV for sulfates. It should also be noted that the atomic ratio between S (metal-sulfide) to Mo (MoS $_x$) remained close to 2.1; while for Cl 2p (Fig. S22c), no peaks can be discerned, indicating the loss of the Cl residues on MS-200. These results suggest that the Mo-S moieties most likely served as the dominant active sites for HER.

Note that 10 s (MS-200 was prepared by heating the precursors at 200 A for 10 s) also represented the optimal heating time. At the same heating current of 200 A, samples prepared for a shorter (5 s) or longer (20 s) heating time yielded only a reduced performance (Fig. S23), with η_{10} of -218 and -250 mV, respectively. This is likely because prolonged heating enhanced sample crystallization, while too short a heating time resulted in a low temperature and hence insufficient decomposition of the precursors. Notably, MS-200 stood out as one of the top Mo-S based HER catalysts as compared to relevant nanocomposites in the literature (Table S10). Yet the preparation of MS-200 took only seconds, in stark contrast to hours typically needed for others prepared using conventional thermal methods.

3.4. DFT study

To understand the mechanistic contributions to the HER activity, DFT calculations were carried out to study the energetics of H adsorption on the proposed subunit of amorphous MoS $_x$ and crystalline MoS $_2$ (Fig. 6a). Considering that Cl could be attacked by protons, as evidenced by experimental and theoretical results that Mo-Cl may be broken forming Cl-H bonds (Fig. S24), blocks with various Cl coordination including Mo $_3$ S $_7$ Cl $_6$, Mo $_3$ S $_7$ Cl $_4$, Mo $_3$ S $_7$ Cl $_2$, and Mo $_3$ S $_7$ were constructed in the calculations. The total density of states (DOS) of all models was first examined. As shown in Fig. 6b, except for the basal planes of MoS $_2$, all other models contain states at the Fermi level contributed from the d orbitals of the Mo atoms. This implies that they all have metallic, rather than semiconducting, features, like the edge of MoS $_2$ [22]. Fig. 6c depicts the energetics of H adsorption (ΔG_{H^*}) on the S and Mo sites of

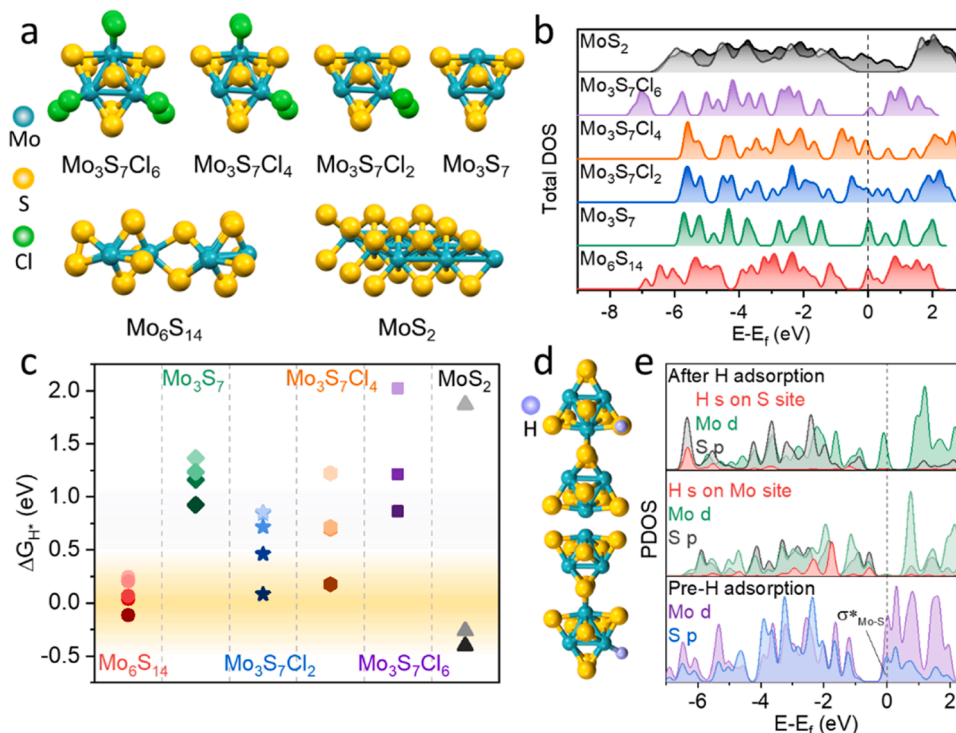


Fig. 6. (a) Calculation models of Mo $_3$ S $_7$ Cl $_6$, Mo $_3$ S $_7$ Cl $_4$, Mo $_3$ S $_7$ Cl $_2$, Mo $_3$ S $_7$, Mo $_6$ S $_{14}$, and MoS $_2$. (b) The corresponding total density of states (DOS) and (c) Gibbs free energies of H adsorption on the various models. Note that the total DOS of the basal plane and the edge of MoS $_2$ are shaded in grey and black in (b), respectively. H adsorptions on MoS $_2$ are calculated separately on the basal plane and the edge. (d) Most suitable H adsorption on the S (upper, site III in Fig. S31) and Mo (lower, site V in Fig. S31) sites on Mo $_6$ S $_{14}$, and (e) the projected DOS (PDOS) of H s, Mo d, S p orbitals, and PDOS of Mo d, S p before H adsorption. Dashed curves in (b) and (e) represent the position of the Fermi level (E $_f$).

the various models (Fig. S25–S31), where the shaded region denotes the optimal range of ΔG_{H^*} for HER. For benchmarking, crystalline MoS_2 was first examined for H adsorption on its basal plane and edge sites. One can see that the S site of the basal plane of crystalline MoS_2 exhibits a high ΔG_{H^*} of 1.87 eV (Fig. S25), denoting the significant difficulty for H adsorption. In contrast, for both Mo or S edge sites, ΔG_{H^*} is diminished to -0.40 and -0.26 eV (Fig. S26), respectively, much closer to the ideal ΔG_{H^*} of 0 eV. This is indeed consistent with widely reported results that the edge of MoS_2 provides the main active sites of HER [5,70]. The $\text{Mo}_3\text{S}_7\text{Cl}_6$ cluster was then studied. One can see from Fig. S27 that the ΔG_{H^*} on apical S is 2.02 eV (Site I), close to that on the basal plane S of crystalline MoS_2 (Fig. S25). As for bridging disulfides, though significantly lower than the apical one, with a ΔG_{H^*} of 0.87 (Site II) and 1.21 eV (Site III), respectively, they are still too high for H adsorption (Fig. 6c). Interestingly, if $\text{Mo}_3\text{S}_7\text{Cl}_6$ loses two Cl atoms into $\text{Mo}_3\text{S}_7\text{Cl}_4$, the Mo atom will be exposed, featuring a low ΔG_{H^*} of 0.18 eV (Site II, Fig. S28) that suggests a markedly better adsorption site for H than the MoS_2 edge. However, apical S (Site I) or bridging S_2 (Site III–VI) of the cluster still possesses too high an adsorption energy for H (0.7–1.2 eV). If a further deprivation of Cl atoms occurs on $\text{Mo}_3\text{S}_7\text{Cl}_4$, the apical S of the yielded $\text{Mo}_3\text{S}_7\text{Cl}_2$ cluster now exhibits a near-zero ΔG_{H^*} of 0.09 eV (Site I, Fig. S29), whereas the exposed Mo site (Site II, $\Delta G_{H^*} = 0.46$ eV) becomes worse than that of $\text{Mo}_3\text{S}_7\text{Cl}_4$ (0.18 eV). Other bridging S_2 sites still manifest too high a ΔG_{H^*} of 0.7–0.9 eV (Site III–VI). In the extreme case, without any Cl atoms, the S and Mo sites of the Mo_3S_7 cluster show a ΔG_{H^*} over 0.9 eV, and are unlikely to be the active sites for HER (Fig. S30).

Nevertheless, considering that the post-electrochemistry XPS measurements showed a complete loss of Cl residues from the samples, these basic MoS_x clusters likely undergo structural aggregation, with unsaturated Mo sites and bridging S_2 . Therefore, dimeric Mo_6S_{14} was built by the aggregation of two Mo_3S_7 clusters (Fig. 6a). In fact, when the exposed Mo of one cluster is combined with the bridging S_2 of another, the S–S bond is dissociated to coordinate with Mo, which is consistent with the XPS results that the bridging S_2 peaks diminished after HER reactions. Also, the Mo to S atomic ratio (7:3) is close to 2.1, based on XPS results. Several S and Mo sites of Mo_6S_{14} are examined and all are shown to be suitable sites for HER (Fig. 6c and S31), where the Mo site (Site V) exhibits a low ΔG_{H^*} of 0.07 eV and one S site (Site III) shows a ΔG_{H^*} of 0.04 eV. In addition, note that the apical S of Mo_6S_{14} and $\text{Mo}_3\text{S}_7\text{Cl}_2$ all relaxed into an edge S-like fashion after H adsorption, which may account for the diminishing apical S in XPS measurements (Fig. 3b). Overall, it can be seen that whereas $\text{Mo}_3\text{S}_7\text{Cl}_x$ ($x = 2, 4$) and Mo_6S_{14} all possess ΔG_{H^*} lower than that of the basal plane of crystalline MoS_2 (Fig. 6c), Mo_6S_{14} is most likely the dominant structure responsible for the HER activity, with the formation facilitated by the depletion of Cl residues during electrochemical operation. This is indeed consistent with the Tafel analysis (Fig. 5b) that the rate-determining step changed from the Heyrovsky step for MS-200 to the Volmer step for MS-600, as the H became energetically difficult to adsorb onto the crystalline MoS_2 [18].

To gain deeper insights into the underlying mechanisms, projected density of states (PDOS) was derived from these models to examine the characteristics of each elemental orbital both before and after hydrogen adsorption. From Fig. S32–S33, it can be seen that the S p orbitals of bridging S_2 and apical S exhibit similar distributions to those in the basal plane of MoS_2 , rather than the edge S atoms. These orbitals display an increasing number of states farther away from the Fermi level, resulting in poor H adsorption on these sites. However, there is an exception for the apical S atom in $\text{Mo}_3\text{S}_7\text{Cl}_2$, which exhibits a low ΔG_{H^*} of 0.09 eV. This exception may be attributed to the significant decrease in Mo–S (d-p orbitals) antibonding states (σ^*) near the Fermi level upon H adsorption on the S site (Fig. S34). This would enhance the stability of the cluster and contribute to its favorable adsorption of H. In contrast, all other clusters display newly formed antibonding states of S–H (p-s orbitals) at the Fermi level, resulting in increased system energies (Fig. S35) [9,14,

71]. This phenomenon explains the high ΔG_{H^*} values observed on the S atoms in the basal plane of MoS_2 due to the generation of H antibonding states (Fig. S35). Conversely, such effects do not occur on the edge S atoms of MoS_2 (Fig. S36). In the case of Mo_6S_{14} , Fig. 6d (upper) illustrates the most suitable S site for H adsorption. The corresponding PDOS in Fig. 6e reveals upward shifts and a significant reduction in the filled states of Mo–S antibonding states at the Fermi level, indicating that H adsorption enhances the stability of the system, leading to a favorable ΔG_{H^*} . This observation is consistent with other S sites (Fig. S37–S38) and can account for the superior ΔG_{H^*} values depicted in Fig. 6c. Furthermore, Mo as catalytic sites was evaluated by analyzing the PDOS of the Mo d orbitals and the corresponding d-band center (Fig. S39–S40). For clusters, the ΔG_{H^*} values follow a linear relation to the d-band center that a closer d-band center can lead to a stronger H adsorption [72,73]. Note that the MoS_2 –Mo edge site (Fig. S41) and Mo_6S_{14} do not follow this trend, possibly due to their relatively stronger structural stability to these smaller clusters [9]. Like the S sites of Mo_6S_{14} , when H is bonded to the exposed Mo site (Fig. 6d, lower), the Mo–S antibonding states at the Fermi level are drastically diminished. In summary, these results show that hydrogen adsorption can be influenced by the H and Mo–S antibonding states, which significantly impact the stability of the system.

4. Conclusion

In this study, MIH was employed for the rapid preparation (only 10 s) of carbon-supported MoS_x composites. The materials exhibited an apparent amorphous to crystalline structural transition with increasing magnetic induction current (heating temperature), as manifested in a range of structural characterizations. Among the series, the sample prepared at 200 A consisted largely of amorphous MoS_x with rich Cl residues, featuring a structure resembling the $\text{Mo}_3\text{S}_7\text{Cl}_4$ cluster, due to incomplete thermal decomposition of the precursors, which was challenging to obtain using traditional pyrolysis method. Therefore, MS-200 stood out as the best HER catalyst in acid with a low η_{10} of only -184 mV. In contrast, the samples prepared at higher MH currents exhibited a mostly crystalline MoS_2 structure and required a much higher η_{10} (over -340 mV). DFT studies showed that optimal H^* absorption occurred on the Mo and S sites of amorphous MoS_x , instead of the basal planes of crystalline MoS_2 , and the $\text{Mo}_3\text{S}_7\text{Cl}_x$ ($x = 2, 4$) and Mo_6S_{14} dimeric cluster units were identified as the preferred HER active sites. In conjunction with experimental results, however, it was found that the HER activity was primarily due to Mo_6S_{14} , where the dimerization was facilitated by the loss of Cl residues of $\text{Mo}_3\text{S}_7\text{Cl}_x$ during electrochemical reaction in acidic media. In summary, these results highlight the unique significance of MIH in the rapid production of defective/nonequilibrium nanocomposites for enhanced electrocatalytic performance. In particular, this can be integrated with other structural engineering strategies for further improvement of the performance, such as heteroatom/metal doping, metal-support interaction, etc., such that the samples can also be used for other energy storage technologies and environmental applications [15]. Relevant research is ongoing and results will be reported in due course.

CRediT authorship contribution statement

Qiming Liu: Data curation, Formal analysis, Writing – original draft. **Forrest Nichols:** Data curation, Formal analysis. **Amrinder Bhuller:** Data curation. **Kevin Singewald:** Data curation, Formal analysis. **Han-Lin Kuo:** Data curation. **Jennifer Q. Lu:** Formal analysis. **Glenn L. Millhauser:** Formal analysis. **Frank Bridges:** Data curation, Formal analysis. **Qingfeng Ge:** Data curation, Formal analysis, Methodology. **Shaowei Chen:** Conceptualization, Formal analysis, Funding acquisition, Writing – review & editing.

Declaration of Competing Interest

The authors declare that they have no known competing financial interests or personal relationships that could have appeared to influence the work reported in this paper.

Data Availability

Data will be made available on request.

Acknowledgements

The work was supported by the National Science Foundation (CHE-1900235 and CHE-2003685). Raman, TEM and XPS work were carried out at the National Center for Electron Microscopy and Molecular Foundry, Lawrence Berkeley National Laboratory, which is supported by the US Department of Energy under Contract No. DE-AC02-05CH11231, as part of a user project. XAS work was carried out at the Stanford Synchrotron Radiation Lightsource (SSRL), which is supported by the U. S. Department of Energy, Office of Science, Office of Basic Energy Sciences under contract no. DE-AC02-76SF00515. Part of the computational work was carried out using the UCSC Lux Supercomputer which is funded by the NSF MRI program (AST-1828315).

Appendix A. Supporting information

Supplementary data associated with this article can be found in the online version at doi:10.1016/j.apcatb.2023.123399.

References

- [1] Z.W. Seh, J. Kibsgaard, C.F. Dickens, I.B. Chorkendorff, J.K. Nørskov, T. F. Jaramillo, Combining theory and experiment in electrocatalysis: Insights into materials design, *Science* 355 (2017), eaad4998.
- [2] M. Chatenet, B.G. Pollet, D.R. Dekel, F. Dionigi, J. Deseure, P. Millet, R.D. Braatz, M.Z. Bazant, M. Eikerling, I. Staffell, P. Balcombe, Y. Shao-Horn, H. Schafer, Water electrolysis: from textbook knowledge to the latest scientific strategies and industrial developments, *Chem. Soc. Rev.* 51 (2022) 4583–4762.
- [3] X.X. Zou, Y. Zhang, Noble metal-free hydrogen evolution catalysts for water splitting, *Chem. Soc. Rev.* 44 (2015) 5148–5180.
- [4] L.B. Xie, L.L. Wang, W.W. Zhao, S.J. Liu, W. Huang, Q. Zhao, WS₂ moire superlattices derived from mechanical flexibility for hydrogen evolution reaction, *Nat. Commun.* 12 (2021) 5070.
- [5] Y. Cao, Roadmap and direction toward high-performance MoS₂ hydrogen evolution catalysts, *ACS Nano* 15 (2021) 11014–11039.
- [6] T.F. Jaramillo, K.P. Jørgensen, J. Bonde, J.H. Nielsen, S. Hørch, I. Chorkendorff, Identification of active edge sites for electrochemical H₂ evolution from MoS₂ nanocatalysts, *Science* 317 (2007) 100–102.
- [7] C. Sun, L.L. Wang, W.W. Zhao, L.B. Xie, J. Wang, J.M. Li, B.X. Li, S.J. Liu, Z. C. Zhuang, Q. Zhao, Atomic-level design of active site on two-dimensional MoS₂ toward efficient hydrogen evolution: experiment, theory, and artificial intelligence modelling, *Adv. Funct. Mater.* 32 (2022) 2206163.
- [8] W.Y. Chen, Z. Wang, K.V. Bets, D.X. Luong, M.Q. Ren, M.G. Stanford, E.A. McHugh, W.A. Algozeeb, H. Guo, G.H. Gao, B. Deng, J.H. Chen, J.T. Li, W.T. Carsten, B. I. Yakobson, J.M. Tour, Millisecond Conversion of Metastable 2D Materials by Flash Joule Heating, *ACS Nano* 15 (2021) 1282–1290.
- [9] Y.X. Ouyang, C.Y. Ling, Q. Chen, Z.L. Wang, L. Shi, J.L. Wang, Activating Inert Basal Planes of MoS₂ for Hydrogen Evolution Reaction through the Formation of Different Intrinsic Defects, *Chem. Mater.* 28 (2016) 4390–4396.
- [10] L. Li, Z.D. Qin, L. Ries, S. Hong, T. Michel, J. Yang, C. Salameh, M. Bechelany, P. Miele, D. Kaplan, M. Chhowalla, D. Voiry, Role of sulfur vacancies and undercoordinated Mo regions in MoS₂ nanosheets toward the evolution of hydrogen, *ACS Nano* 13 (2019) 6824–6834.
- [11] T. Sun, J. Wang, X. Chi, Y.X. Lin, Z.X. Chen, X. Ling, C.T. Qiu, Y.S. Xu, L. Song, W. Chen, C.L. Su, Engineering the electronic structure of MoS₂ nanorods by N and Mn dopants for ultra-efficient hydrogen production, *ACS Catal.* 8 (2018) 7585–7592.
- [12] Q. Liu, Z.Q. Xue, B.M. Jia, Q.L. Liu, K. Liu, Y.Y. Lin, M. Liu, Y.L. Li, G.Q. Li, Hierarchical nanorods of MoS₂/MoP heterojunction for efficient electrocatalytic hydrogen evolution reaction, *Small* 16 (2020) 2002482.
- [13] J. Joyner, E.F. Oliveira, H. Yamaguchi, K. Kato, S. Vinod, D.S. Galvao, D. Salpekar, S. Roy, U. Martinez, C.S. Tiwary, S. Ozden, P.M. Ajayan, Graphene supported MoS₂ structures with high defect density for an efficient HER electrocatalysts, *ACS Appl. Mater. Interfaces* 12 (2020) 12629–12638.
- [14] C. Tsai, F. Abild-Pedersen, J.K. Nørskov, Tuning the MoS₂ edge-site activity for hydrogen evolution via support interactions, *Nano Lett.* 14 (2014) 1381–1387.
- [15] C. Chang, L.L. Wang, L.B. Xie, W.W. Zhao, S.J. Liu, Z.C. Zhuang, S.J. Liu, J.M. Li, X. Liu, Q. Zhao, Amorphous molybdenum sulfide and its Mo-S motifs: structural characteristics, synthetic strategies, and comprehensive applications, *Nano Res.* 15 (2022) 8613–8635.
- [16] Y.M. He, L.R. Liu, C. Zhu, S.S. Guo, P. Golani, B. Koo, P.Y. Tang, Z.Q. Zhao, M. Z. Xu, P. Yu, X. Zhou, C.T. Gao, X.W. Wang, Z.D. Shi, L. Zheng, J.F. Yang, B. Shin, J. Arbiol, H.G. Duan, Y.H. Du, M. Heggen, R.E. Dunin-Borkowski, W.L. Guo, Q. J. Wang, Z.H. Zhang, Z. Liu, Amorphizing noble metal chalcogenide catalysts at the single-layer limit towards hydrogen production, *Nat. Catal.* 5 (2022) 212–221.
- [17] B. Seo, G.Y. Jung, S.J. Lee, D.S. Baek, Y.J. Sa, H.W. Ban, J.S. Son, K. Park, S. K. Kwak, S.H. Joo, Monomeric MoS₄²⁻-derived polymeric chains with active molecular units for efficient hydrogen evolution reaction, *ACS Catal.* 10 (2020) 652–662.
- [18] M.L. Grutza, A. Rajagopal, C. Streb, P. Kurz, Hydrogen evolution catalysis by molybdenum sulfides (MoS_x): are thiomolybdate clusters like [Mo₃S₁₃]²⁻ suitable active site models? *Sustain. Energy Fuels* 2 (2018) 1893–1904.
- [19] T.F. Jaramillo, J. Bonde, J.D. Zhang, B.L. Ooi, K. Andersson, J. Ulstrup, I. Chorkendorff, Hydrogen evolution on supported incomplete cubane-type [Mo₃S₄]⁴⁺ electrocatalysts, *J. Phys. Chem. C* 112 (2008) 17492–17498.
- [20] J. Kibsgaard, T.F. Jaramillo, F. Besenbacher, Building an appropriate active-site motif into a hydrogen-evolution catalyst with thiomolybdate [Mo₃S₁₃]²⁻ clusters, *Nat. Chem.* 6 (2014) 248–253.
- [21] J.D. Benck, Z.B. Chen, L.Y. Kuritzky, A.J. Forman, T.F. Jaramillo, Amorphous molybdenum sulfide catalysts for electrochemical hydrogen production: insights into the origin of their catalytic activity, *ACS Catal.* 2 (2012) 1916–1923.
- [22] L.F. Wu, A. Longo, N.Y. Dzade, A. Sharma, M.M.R.M. Hendrix, A.A. Bol, N.H. de Leeuw, E.J.M. Hensen, J.P. Hofmann, The origin of high activity of amorphous MoS₂ in the hydrogen evolution reaction, *ChemSusChem* 12 (2019) 4383–4389.
- [23] B. Lu, Q. Liu, C. Wang, Z. Masood, D.J. Morris, F. Nichols, R. Mercado, P. Zhang, Q. Ge, H.L. Xin, S. Chen, Ultrafast preparation of nonequilibrium FeNi spinels by magnetic induction heating for unprecedented oxygen evolution electrocatalysis, *Research* (2022) 9756983.
- [24] Q.M. Liu, B.Z. Lu, F. Nichols, J. Ko, R. Mercado, F. Bridges, S.W. Chen, Rapid preparation of carbon-supported ruthenium nanoparticles by magnetic induction heating for efficient hydrogen evolution reaction in both acidic and alkaline media, *Susmat* 2 (2022) 335–346.
- [25] Q. Liu, S. McNair, F. Nichols, B. Lu, B. Yu, D. Pan, J. Ko, A. Bhuller, F. Bridges, S. Chen, Ultrafast synthesis of cobalt/carbon nanocomposites by magnetic induction heating for oxygen evolution reaction, *Adv. Sens. Energy Mater.* 2 (2023), 100046.
- [26] Q.M. Liu, S.W. Chen, Ultrafast synthesis of electrocatalysts, *Trends Chem.* 4 (2022) 918–934.
- [27] R. Jiang, Y.M. Da, X.P. Han, Y.A. Chen, Y.D. Deng, W.B. Hu, Ultrafast Synthesis for Functional Nanomaterials, *Cell Rep. Phys. Sci.* 2 (2021), 100302.
- [28] C. Booth, F. Bridges, Real-Space X-ray Absorption Package (RSXAP), *Intl Tables Crystal* 1 (2021), <https://doi.org/10.1107/S1547487020003444>.
- [29] P. Giannozzi, S. Baroni, N. Bonini, M. Calandra, R. Car, C. Cavazzoni, D. Ceresoli, G.L. Chiarotti, M. Cococcioni, I. Dabo, A. Dal Corso, S. de Gironcoli, S. Fabris, G. Fratesi, R. Gebauer, U. Gerstmann, C. Gougousis, A. Kokalj, M. Lazzeri, L. Martin-Samos, N. Marzari, F. Mauri, R. Mazzarello, S. Paolini, A. Pasquarello, L. Paulatto, C. Sbraccia, S. Scandolo, G. Sclauzero, A.P. Seitsonen, A. Smogunov, P. Umari, R.M. Wentzcovitch, QUANTUM ESPRESSO: a modular and open-source software project for quantum simulations of materials, *J. Phys. -Condens Mat.* 21 (2009), 395502.
- [30] K.F. Garrity, J.W. Bennett, K.M. Rabe, D. Vanderbilt, Pseudopotentials for high-throughput DFT calculations, *Comput. Mater. Sci.* 81 (2014) 446–452.
- [31] S. Grimme, J. Antony, S. Ehrlich, H. Krieg, A consistent and accurate ab initio parametrization of density functional dispersion correction (DFT-D) for the 94 elements H-Pu, *J. Chem. Phys.* 132 (2010), 154104.
- [32] S. Baroni, S. de Gironcoli, A. Dal Corso, P. Giannozzi, Phonons and related crystal properties from density-functional perturbation theory, *Rev. Mod. Phys.* 73 (2001) 515–562.
- [33] M.J. Frisch, G.W. Trucks, H.B. Schlegel, G.E. Scuseria, M.A. Robb, J.R. Cheeseman, G. Scalmani, V. Barone, G.A. Petersson, H. Nakatsuji, X. Li, M. Caricato, A. V. Marenich, J. Bloino, B.G. Janesko, R. Gomperts, B. Mennucci, H.P. Hratchian, J. V. Ortiz, A.F. Izmaylov, J.L. Sonnenberg, Williams, F. Ding, F. Lipparini, F. Egidi, J. Goings, B. Peng, A. Petrone, T. Henderson, D. Ranasinghe, V.G. Zakrzewski, J. Gao, N. Rega, G. Zheng, W. Liang, M. Hada, M. Ehara, K. Toyota, R. Fukuda, J. Hasegawa, M. Ishida, T. Nakajima, Y. Honda, O. Kitao, H. Nakai, T. Vreven, K. Throssell, J.A. Montgomery Jr., J.E. Peralta, F. Ogliaro, M.J. Bearpark, J. J. Heyd, E.N. Brothers, K.N. Kudin, V.N. Staroverov, T.A. Keith, R. Kobayashi, J. Normand, K. Raghavachari, A.P. Rendell, J.C. Burant, S.S. Iyengar, J. Tomasi, M. Cossi, J.M. Millam, M. Klene, C. Adamo, R. Cammi, J.W. Ochterski, R.L. Martin, K. Morokuma, O. Farkas, J.B. Foresman, D.J. Fox, C.01, Wallingford, CT, 16 Rev., Gaussian., 2016.
- [34] K.A. Peterson, D. Figgen, M. Dolg, H. Stoll, Energy-consistent relativistic pseudopotentials and correlation consistent basis sets for the 4d elements Y-Pd, *J. Chem. Phys.* 126 (2007) 124101.
- [35] H. Deng, C. Zhang, Y.C. Xie, T. Tumlin, L. Giri, S.P. Karna, J. Lin, Laser induced MoS₂/carbon hybrids for hydrogen evolution reaction catalysts, *J. Mater. Chem. A* 4 (2016) 6824–6830.
- [36] Y.L. Pan, L.L. Gong, X.D. Cheng, Y. Zhou, Y.B. Fu, J. Feng, H. Ahmed, H.P. Zhang, Layer-spacing-enlarged MoS₂ superstructural nanotubes with further enhanced catalysis and immobilization for Li-S batteries, *ACS Nano* 14 (2020) 5917–5925.
- [37] X. Wang, Y.W. Zhang, H.N. Si, Q.H. Zhang, J. Wu, L. Gao, X.F. Wei, Y. Sun, Q. L. Liao, Z. Zhang, K. Ammarah, L. Gu, Z. Kang, Y. Zhang, Single-atom vacancy

- defect to trigger high-efficiency hydrogen evolution of MoS₂, *J. Am. Chem. Soc.* 142 (2020) 4298–4308.
- [38] J.C. Park, H. Song, Synthesis of polycrystalline Mo/MoO_x nanoflakes and their transformation to MoO₃ and MoS₂ nanoparticles, *Chem. Mater.* 19 (2007) 2706–2708.
- [39] J. Zhang, T. Wang, D. Pohl, B. Rellinghaus, R.H. Dong, S.H. Liu, X.D. Zhuang, X. L. Feng, Interface engineering of MoS₂/Ni₃S₂ heterostructures for highly enhanced electrochemical overall-water-splitting activity, *Angew. Chem. Int. Ed.* 55 (2016) 6702–6707.
- [40] X.W. Zhang, F. Meng, S. Mao, Q. Ding, M.J. Shearer, M.S. Faber, J.H. Chen, R. J. Hamers, S. Jin, Amorphous MoS₂Cl₂ electrocatalyst supported by vertical graphene for efficient electrochemical and photoelectrochemical hydrogen generation, *Energ. Environ. Sci.* 8 (2015) 862–868.
- [41] Y.H. Chang, C.T. Lin, T.Y. Chen, C.L. Hsu, Y.H. Lee, W.J. Zhang, K.H. Wei, L.J. Li, Highly efficient electrocatalytic hydrogen production by MoS_x grown on graphene-protected 3D Ni foams, *Adv. Mater.* 25 (2013) 756–760.
- [42] H.J.W. Li, C. Cai, Q.Y. Wang, S.Y. Chen, J.W. Fu, B. Liu, Q.N. Hu, K.M. Hu, H.M. Li, J.H. Hu, Q.M. Liu, S.W. Chen, M. Liu, High-performance alkaline water splitting by Ni nanoparticle-decorated Mo-Ni microrods: Enhanced ion adsorption by the local electric field, *Chem. Eng. J.* 435 (2022), 134860.
- [43] J.L. Liu, W.X. Cheng, K.T. Zhang, H. Liu, J.Q. Li, J. Tressel, S.W. Chen, High-efficiency photodynamic antibacterial activity of NH₂-MIL-101(Fe)/MoS₂/ZnO ternary composites, *ACS Appl. Bio Mater.* 5 (2022) 3912–3922.
- [44] Y. Yang, H.L. Fei, G.D. Ruan, C.S. Xiang, J.M. Tour, Edge-oriented MoS₂ nanoporous films as flexible electrodes for hydrogen evolution reactions and supercapacitor devices, *Adv. Mater.* 26 (2014) 8163–8168.
- [45] A. Morozan, H. Johnson, C. Roiron, G. Genay, D. Aldakov, A. Ghedjatti, C. T. Nguyen, P.D. Tran, S. Kinge, V. Artero, Nonprecious bimetallic iron-molybdenum sulfide electrocatalysts for the hydrogen evolution reaction in proton exchange membrane electrolyzers, *ACS Catal.* 10 (2020) 14336–14348.
- [46] M. Dave, A. Rajagopal, M. Damm-Ruttensperger, B. Schwarz, F. Nagele, L. Daccache, D. Fantauzzi, T. Jacob, C. Streb, Understanding homogeneous hydrogen evolution reactivity and deactivation pathways of molecular molybdenum sulfide catalysts, *Sustain. Energy Fuels* 2 (2018) 1020–1026.
- [47] H.L. Ye, L. Wang, S. Deng, X.Q. Zeng, K.Q. Nie, P.N. Duchesne, B. Wang, S. Liu, J. H. Zhou, F.P. Zhao, N. Han, P. Zhang, J. Zhong, X.H. Sun, Y.Y. Li, Y.G. Li, J. Lu, Amorphous MoS₃ infiltrated with carbon nanotubes as an advanced anode material of sodium-ion batteries with large gravimetric, areal, and volumetric capacities, *Adv. Energy Mater.* 7 (2017) 1601602.
- [48] Q.M. Liu, Y. Peng, Q.X. Li, T. He, D. Morris, F. Nichols, R. Mercado, P. Zhang, S. W. Chen, Atomic dispersion and surface enrichment of palladium in nitrogen-doped porous carbon cages lead to high-performance electrocatalytic reduction of oxygen, *ACS Appl. Mater. Interfaces* 12 (2020) 17641–17650.
- [49] Q.M. Liu, H.B. Zhou, F. Nichols, H.L. Kuo, R. Mercado, B.Z. Lu, W.Y. Zhu, Y.S. Liu, J.Q. Lu, F. Bridges, S.W. Chen, Oxygen reduction reaction catalyzed by carbon composites with ruthenium-doped iron oxide nanoparticles, *Mater. Adv.* 3 (2022) 4556–4565.
- [50] B.Z. Yu, Q.M. Liu, F. Nichols, K. Mayford, D.J. Pan, H.L. Kuo, J.Q. Lu, F. Bridges, S. W. Chen, Platinum-anchored iron oxide nanostructures for efficient hydrogen evolution reaction in acidic media, *J. Phys. Chem. C* (2023) 3996–4005.
- [51] B.Z. Lu, C.B. Wahl, X.K. Lu, M.E. Sweers, H.F. Li, V.P. Dravid, L.C. Seitz, Iridium-incorporated strontium tungsten oxynitride perovskite for efficient acidic hydrogen evolution, *J. Am. Chem. Soc.* 144 (2022) 13547–13555.
- [52] B.G. Silbernagel, Electron-Spin Resonance of Sulfide Catalysts, *J. Magn. Magn. Mater.* 31–34 (1983) 885–886.
- [53] P.D. Tran, T.V. Tran, M. Orio, S. Torelli, Q.D. Truong, K. Nayuki, Y. Sasaki, S. Y. Chiam, R. Yi, I. Honma, J. Barber, V. Artero, Coordination polymer structure and revisited hydrogen evolution catalytic mechanism for amorphous molybdenum sulfide, *Nat. Mater.* 15 (2016) 640–646.
- [54] J.A. Bau, A.H. Emwas, P. Nikolaenko, A.A. Aljarb, V. Tung, M. Rueping, Mo³⁺ hydride as the common origin of H₂ evolution and selective NADH regeneration in molybdenum sulfide electrocatalysts, *Nat. Catal.* 5 (2022) 397–404.
- [55] Y.L. Zhou, Y.Y. Li, Q.Q. Wang, Q. Wang, R. Du, M. Zhang, X.Q. Sun, X.Y. Zhang, L. T. Kang, F.Y. Jiang, Ultrasmall MoS₃ loaded GO nanocomposites as high-rate and long-cycle-life anode materials for lithium- and sodium-ion batteries, *ChemElectroChem* 6 (2019) 3113–3119.
- [56] H. Li, Q. Zhang, C.C.R. Yap, B.K. Tay, T.H.T. Edwin, A. Olivier, D. Baillargeat, From Bulk to Monolayer MoS₂: Evolution of Raman Scattering, *Adv. Funct. Mater.* 22 (2012) 1385–1390.
- [57] X. Luo, Y.Y. Zhao, J. Zhang, Q.H. Xiong, S.Y. Quek, Anomalous frequency trends in MoS₂ thin films attributed to surface effects, *Phys. Rev. B* 88 (2013), 075320.
- [58] V.Y. Fominiski, R.I. Romanov, D.V. Fominiski, A.V. Shelyakov, Regulated growth of quasi-amorphous MoS_x thin-film hydrogen evolution catalysts by pulsed laser deposition of Mo in reactive H₂S gas, *Thin Solid Films* 642 (2017) 58–68.
- [59] Y.M. Li, R. Nakamura, Structural change of molybdenum sulfide facilitates the electrocatalytic hydrogen evolution reaction at neutral pH as revealed by in situ Raman spectroscopy, *Chin. J. Catal.* 39 (2018) 401–406.
- [60] S. Takenaka, T. Tanaka, T. Funabiki, S. Yoshida, Structures of molybdenum species in silica-supported molybdenum oxide and alkali-ion-modified silica-supported molybdenum oxide, *J. Phys. Chem. B* 102 (1998) 2960–2969.
- [61] B. Lassalle-Kaiser, D. Merki, H. Vrubel, S. Gul, V.K. Yachandra, X.L. Hu, J. Yano, Evidence from in Situ X-ray absorption spectroscopy for the involvement of terminal disulfide in the reduction of protons by an amorphous molybdenum sulfide electrocatalyst, *J. Am. Chem. Soc.* 137 (2015) 314–321.
- [62] F. Jililehvand, B.S. Lim, R.H. Holm, B. Hedman, K.O. Hodgson, X-ray absorption spectroscopy of a structural analogue of the oxidized active sites in the sulfite oxidase enzyme family and related molybdenum(V) complexes, *Inorg. Chem.* 42 (2003) 5531–5536.
- [63] S.I. Zabinsky, J.J. Rehr, A. Ankudinov, R.C. Albers, M.J. Eller, Multiple-scattering calculations of X-ray-absorption spectra, *Phys. Rev. B* 52 (1995) 2995–3009.
- [64] Q. Liu, Q. Fang, W.S. Chu, Y.Y. Wan, X.L. Li, W.Y. Xu, M. Habib, S. Tao, Y. Zhou, D. B. Liu, T. Xiang, A. Khalil, X.J. Wu, M. Chhowalla, P.M. Ajayan, L. Song, Electron-doped 1T-MoS₂ via interface engineering for enhanced electrocatalytic hydrogen evolution, *Chem. Mater.* 29 (2017) 4738–4744.
- [65] Y. Shi, Y. Zhou, D.R. Yang, W.X. Xu, C. Wang, F.B. Wang, J.J. Xu, X.H. Xia, H. Y. Chen, Energy level engineering of MoS₂ by transition-metal doping for accelerating hydrogen evolution reaction, *J. Am. Chem. Soc.* 139 (2017) 15479–15485.
- [66] F.X. Xi, P. Bogdanoff, K. Harbauer, P. Plate, C. Holm, J. Rappich, B. Wang, X. Y. Han, R. van de Krol, S. Fiechter, Structural transformation identification of sputtered amorphous MoS_x as an efficient hydrogen-evolving catalyst during electrochemical activation, *ACS Catal.* 9 (2019) 2368–2380.
- [67] X.Y. Tian, P.C. Zhao, W.C. Sheng, Hydrogen evolution and oxidation: mechanistic studies and material advances, *Adv. Mater.* 31 (2019) 1808066.
- [68] Z.B. Chen, D. Cummins, B.N. Reinecke, E. Clark, M.K. Sunkara, T.F. Jaramillo, Core-shell MoO₃-MoS₂ nanowires for hydrogen evolution: a functional design for electrocatalytic materials, *Nano Lett.* 11 (2011) 4168–4175.
- [69] Y. Zhou, J. Zhang, E.H. Song, J.H. Lin, J.D. Zhou, K. Suenaga, W. Zhou, Z. Liu, J. J. Liu, J. Lou, H.J. Fan, Enhanced performance of in-plane transition metal dichalcogenides monolayers by configuring local atomic structures, *Nat. Commun.* 11 (2020) 2253.
- [70] A. Bruix, H.G. Fuchtbauer, A.K. Tuxen, A.S. Walton, M. Andersen, S. Porsgaard, F. Besenbacher, B. Hammer, J.V. Lauritsen, In situ detection of active edge sites in single-layer MoS₂ catalysts, *ACS Nano* 9 (2015) 9322–9330.
- [71] Y.X. Sun, Z.G. Wang, Density functional theory study on the hydrogen evolution reaction in the S-rich SnS₂ nanosheets, *Electrocatalysis* 11 (2020) 604–611.
- [72] Y. Peng, Q.M. Liu, B.Z. Lu, T. He, F. Nichols, X. Hu, T. Huang, G. Huang, L. Guzman, Y. Ping, S.W. Chen, Organically capped iridium nanoparticles as high-performance bifunctional electrocatalysts for full water splitting in both acidic and alkaline media: impacts of metal-ligand interfacial interactions, *ACS Catal.* 11 (2021) 1179–1188.
- [73] V. Stamenkovic, B.S. Mun, K.J.J. Mayrhofer, P.N. Ross, N.M. Markovic, J. Rossmeisl, J. Greeley, J.K. Norskov, Changing the activity of electrocatalysts for oxygen reduction by tuning the surface electronic structure, *Angew. Chem. Int. Ed.* 45 (2006) 2897–2901.